International Journal of Refrigeration 146 (2023) 63–73

Contents lists available at ScienceDirect

International Journal of Refrigeration

journal homepage: www.elsevier.com/locate/ijrefrig

Experimental development and optimization of a standing wave thermoacoustic refrigerator using additive manufactured stacks

Développement expérimental et optimization d'un réfrigérateur thermoacoustique à ondes stationnaires utilisant un empilement conçu par fabrication additive

Emanuele Sarpero [a,b,c], Emmanuel Gourdon [b], Davide Borelli [a,*]

[a] *DIME- TEC, Polytechnical School, University of Genoa, Via all' OperaPia 15A, Genoa, 16145 Italy*
[b] *Univ Lyon, ENTPE, École Centrale de Lyon, CNRS, LTDS, UMR 5513, 69518 Vaulx-en-Velin, France*
[c] *Univ Lyon, École Centrale de Lyon, INSA Lyon, Université Claude Bernard Lyon I, CNRS, Laboratoire de Mécanique des Fluides et d'Acoustique, UMR 5509, 36 Avenue Guy de Collongue, F-69134, Ecully, France*

ARTICLE INFO

Keywords:
Thermoacoustics
Acoustic refrigeration
Stack optimization
Additive manufacturing
Standing wave refrigerator

Mots clés:
Thermoacoustique
Froid acoustique
Optimization d'un empilement
Fabrication additive
Réfrigérateur à ondes stationnaires

ABSTRACT

While many previous research publications focused on developing simple and inexpensive acoustic refrigerator prototypes, the current state of play in the field reveals the need to elaborate robust and replicable facilities for experimental and test purposes. In this context, the present article justifies the importance of an economical and technologically simple process demonstrator. The construction of an experimental Thermo-Acoustic Refrigerator (TAR), employing an acoustic-to-thermal energy conversion cycle, is further described. Setup's repeatability and replicability and results' robustness were primarily addressed, while innovative techniques for stack production and optimization were also proposed. The success of experiments in terms of optimization and reproducibility was validated via the temperature gradients obtained. The adequacy of experimental results was verified by comparing them with a numerical simulation using the DeltaEC software.

1. Introduction

In the light of the broadening use of refrigeration in the modern industrial era, and considering that conventional refrigeration fluids such as HCFCs, CFCs and HFCs are listed among the major causes of increased global warming, it seems necessary to implement greener and more sustainable refrigeration solutions in a perspective of gradual replacement of the traditional vapor-compression refrigeration systems. TARs operate with inert non-polluting gasses (e.g., air, helium, argon, etc.), present no frictional losses and require less maintenance costs than ordinary refrigerators. They can operate with either standing or traveling acoustic waves. Standing waves refrigerators are characterized both by the fact that they do not carry energy from one place to another and they also need precise frequencies to operate properly.

It is possible to introduce the ideal thermodynamic cycle of a thermoacoustic refrigerator, in a pressure-volume plane, as depicted in Fig. 1a. The transformations can be explained as follows: an adiabatic isentropic compression (1), an isobaric heat transfer (2), an adiabatic isentropic expansion (3) and an isobaric heat transfer (4).

The basic functioning of a thermoacoustic refrigerator is portrayed in Fig. 1b, where the energy conversion caused by acoustic waves leads to the inverse cycle where Q_c is the module of the heat taken from the cold body at a temperature T_c and Q_h the module of the heat given to the hot body at a temperature T_h. The alternating compression and rarefaction of the gas causes the variation of the local gas temperature. When the local gas temperature increases above the nearby bodies, the heat is transferred from the gas to the wall. On the contrary, when it decreases below the average temperature of the surrounding bodies, the gas gets heated.

Even if the real functioning of the refrigerator could be acceptably compared to the ideal cycle, it is appropriate to introduce the real cycle of an acoustic refrigerator and the relative phases, as depicted in Fig. 1c: a compression caused by the standing sound waves (1), a second phase

* Corresponding author.
E-mail address: davide.borelli@unige.it (D. Borelli).

https://doi.org/10.1016/j.ijrefrig.2022.10.007
Received 25 May 2022; Received in revised form 9 October 2022; Accepted 10 October 2022
Available online 12 October 2022

Nomenclature

Roman symbols

c_p	Specific heat capacity, J·kg^{-1}
f	Frequency, Hz
Pr	Prandtl number, -
Q	Heat module, J
T	Temperature, K
W	Work, W

Greek symbols

δ	Penetration depth, m
k	Gas thermal conductivity, W·m^{-1}·K^{-1}
μ	Dinamic viscosity, g·cm^{-1}· s^{-1}
ω	Angular frequency, rad· s^{-1}
ρ	Density, kg·m^{-3}
Δ	Difference, -

Acronyms

CFCs	Chlorofluorocarbons
HCFCs	Hydrochlorofluorocarbons
HFCs	Hydrofluorocarbons
FEM	Finite Element Method
TAR	Thermo-Acoustic Refrigerator

Subscripts

c	Cold
h	Hot
m	Mean
t	Thermal
v	Viscous

in which heat is given to the stack (2), a rarefaction caused by the standing sound waves (3), and a fourth phase in which heat is absorbed from the stack (4) (Swift, 1999; Rossing, 2007).

For this reason, standing wave TAR prototypes are simpler to build and more economical. Many studies can be found in literature describing the implementation of TARs to address current environmental issues related to classical refrigeration technologies, describing an experimental implementation of a prototype (Russel and Weibull, 2002; Ramadan et al., 2021; Tijani et al., 2002a; Zolpakar et al., 2016; Alcock et al., 2017a; Allesina, 2014; Wetzel and Herman, 1997; Shah et al., 2021) and more complex theory could be found in academic literature (Swift, 1999; Swift, 2002; Crocker, 1997; Rossing, 2007). This study aims to describe the development of a simple and economic prototype, aimed to be robust, easily replicable and innovative from the point of view of the materials chosen, the production techniques and their optimization processes. The parameters coming into play in a TAR are many and complex, but setting in a proper way some design requirements made possible to take into account only some of them, depending on their influence on the model optimization process. The study focuses on the maximum temperature difference (ΔT) obtainable from the optimization of the device, mainly of the stack, without the presence, of heat exchangers. Many problems related to the reproducibility of a TAR are in fact related to the stack, the component that allows the conversion between acoustic energy and heat. Thanks to some of its important parameters such as pore geometry and size, a stack greatly influences the level of its internal temperature if properly designed and constructed with a suitable material. Different studies focus on random stack applications (Bhansali et al., 2015; Yahya et al., 2017), but operating with robust and replicable stacks will allow to focus on their accurate optimization, significantly increasing their performance.

Over the years, thermo-acoustic refrigeration has proven to be an interesting and promising technique due to its low environmental impact and in fields where the noise generated does not represent a sensitive problem, such as in the case of acoustic chillers within automotive projects (Bessis et al., January 2015; Berson et al., 2012), or for climatic-environmental systems in the aerospace field (Garrett et al., 1993). Some prototypes of thermo-acoustic refrigerators for terrestrial and food use have been studied and implemented (Poese et al., 2004), but they have not yet found widespread industrial development due to their efficiency, which is not yet advantageous compared to classical refrigeration techniques.

2. Experimental design and setup

The developed acoustic refrigerator, coherently to the aim of this study, is technologically simple and economical. Being designed to operate with acoustic standing waves, the TAR presents a simple geometry and is based on a modification of a Kundt's tube, sharing its measurement and data acquisition setup. Some modifications were made since this equipment is usually intended to measure acoustic impedance of porous materials and transmission loss. The stack results to be the most complex component of the modified experimental setup and therefore it will be optimized in order to improve the ΔT of the refrigerator.

2.1. Dimensions and components

The experimental configuration is mainly composed of a circular section resonator tube connected to a loudspeaker via a sealed containment box and coupled with a number of electronic devices. In order to provide a detailed description of the apparatus, in Fig. 2a picture of the setup and a sketch of the components are shown, each one named and denoted with an alphabetical letter. The specific nomenclature for each component is also presented in the same sketch.

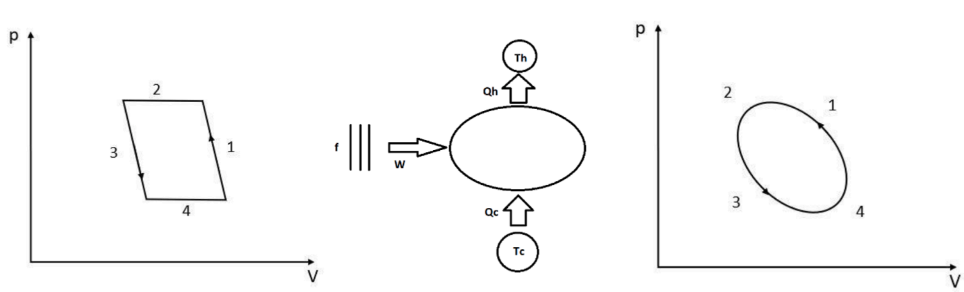

(a) (b) (c)

Fig. 1. TAR inverse cycle in a pressure-volume plane (a), TAR schematic functioning (b) and TAR real cycle in a pressure-volume plane (c).

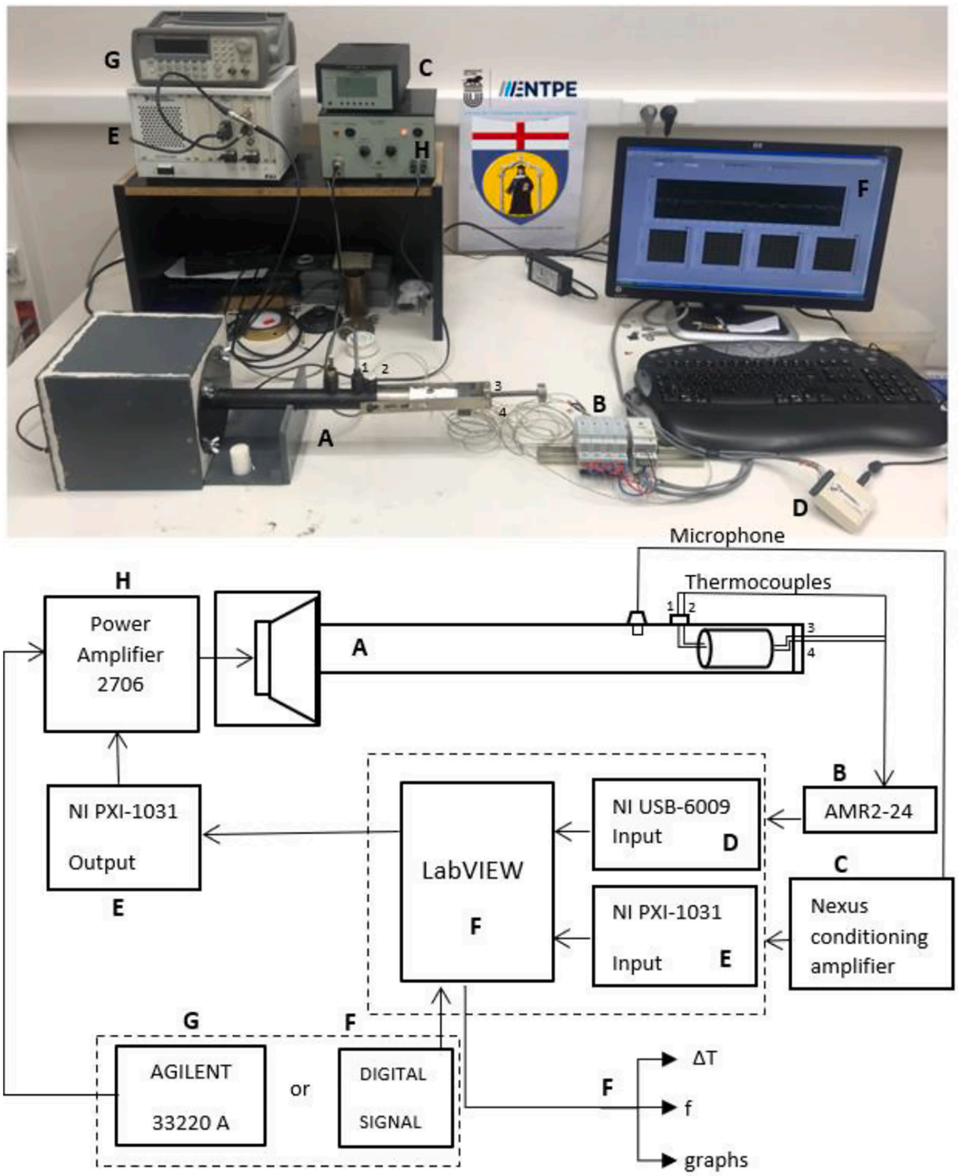

Fig. 2. Experimental Setup image and instrumentation flowchart.

A brass circular section acoustic resonator tube, with a diameter of 29 mm and 390 mm long, is connected to an acoustic driver embedded in a 21.5 × 20.2 × 20.1 cm sealed wooden box. The acoustic source is a classical 8Ω mid-range Visaton loudspeaker. The acoustic power is adjustable depending on the characteristics of the model and of the loudspeaker. The acoustic power of the loudspeaker used in this study, measured with a sound level meter, is equal to 0.229 W. The tube anchorage to the box is secured by a 17 mm diameter metallic plate fixed to the box by four screws and welded to the tube base. The other end of the tube is closed by a plastic plug fixed by a mechanical screw locking. The tube itself presents two parts, the first one fixed and joined to the metallic liner at its base, and a second removable part which enables the insertion of the stack inside the tube. Along the tube surface two holes allow the microphone and the thermocouples to be placed inside the resonator; once positioned, the holes are sealed with a synthetic rubber compound to ensure that the tube is hermetically sealed. It is therefore necessary to evaluate where the maximum of pressure is located inside the resonator in order to obtain the optimal operating conditions. While there are studies that focus on optimizing resonant frequency (Jebali et al., 2004), this study presents a configuration which could be considered as a closed-closed configuration, in which the first pressure node in the tube was measured, giving a tube resonant frequency equal to 193 Hz. Operating at this frequency it was guaranteed to have the optimal resonator acoustic condition.

At this point, using a microphone, it is possible to calculate the average internal pressure of the resonator and the maximum effective pressure. These two values are two fundamental parameters for the understanding of the acoustical phenomenon that takes place inside the tube. In our case, the internal effective acoustic pressure of the resonator is equal to 3.73 Pa, corresponding to 105 dB.

In the case analysed, the used microphones are Brüel & Kjær pressure-field microphones with a sensitivity of 3.72 mV/Pa, connected to a Brüel & Kjær microphone conditioning amplifier (B) and with a National Instrument electronic data acquisition card (E) controlled by a graphical LabVIEW interface (F). Four Crouzet K-type thermocouples, are properly placed at both sides of the stack and connected by a conditioner (B) to a data acquisition card (D). The temperatures are finally acquired by a LabVIEW program (F), whose interface allows to send a digital periodic signal to the loudspeaker via an adjustable power amplifier (H) connected to the user interface by the electronic data acquisition card (E). As an alternative, the signal could be sent to the loudspeaker by a function generator (G). A simple sinusoidal periodic wave signal has been chosen. Regarding the operating fluid, air was chosen to ensure the cost-effectiveness of the model and because of the unlimited availability of this fluid in any laboratory (Nayak et al., 2015). This choice allows to be able to replicate these experiments without onerous costs related to the fluid and to the technical complications that would result from the use of fluids that need controlled atmospheres or very particular sealing conditions such as Helium, Argon or Helium-Argon mixtures, as depicted in literature (Tijani et al., 2002b; Jin et al., 2003) or water vapor (Bekkulov et al., 2020).

2.2. Stack

In a thermoacoustic refrigerator the stack represents the core component of the structure, being the component which allows the energetic exchange between acoustic and thermal energy by means of the air compression and rarefaction inside the empty stack spaces exposed to the acoustic waves. The aim of this study is to have a replicable, robust and inexpensive stack. 3D printing technology allows the production of more robust and cost-effective stacks if compared to random stacks (Yahya et al., 2017) or stacks made of manually assembled filaments and materials (Debojit and Sandip, 2021), or with different materials (Alcock et al., 2017b). With this technology, each stack is precisely reproducible and more robust, a key factor in ensuring the reliability of the results of such experimental campaigns. The production cost of a single stack will be deatailed in Section 3, when the characterization of the stack material will be discussed. Moreover, an optimized stack allows to obtain meaningful temperature differences to be used as heat source in the consequent inverse cycle.

The creation of an additive manufactured stack involves three processes. Firstly, the stack must be designed with an appropriate geometry and dimensions using a CAD software. Once the stack is defined, it is necessary to proceed with the 3D printing of the part, and finally provide a series of post-treatments that clean the stack from any printing residues. In this study, FreeCAD 0.19.3 software was used to design the stacks sections, as shown in the upper part of Fig. 3. The stacks were then printed with a 3D Systems "ProJet 3510 SD" printer using the 3D Multi Jet Printing (MJP) technique, which allows to achieve high resolution by means of a support material (a wax, removed in post processing) and depositing liquid photopolymers onto a build surface using inkjet technology. An average of 10 h is necessary to produce a printed stack sample. The print has a maximum resolution of 375 × 375 × 790 DPI, with 32 μm layers. At the end of the process, the result is a printed stack made of the UV curable plastic material "VisiJet® M3 Crystal" wrapped in a wax backing. In order to melt the wax support both externally and, in particular, internally from the pore channels, it is necessary to proceed with a post-heating process in a static oven at 60 °C in order to obtain a pure stack after about 3 h of treatment. This phase is particularly delicate because at a temperature below 60 °C the wax in the inner interstices cannot be completely melted, while at a higher temperature the stack would undergo a thermoplastic deformation that would compromise its structure and therefore its efficacy. The implemented stacks appear as plastic porous cylinders of 28.75 mm diameter and variable lengths. In a first approach, it was chosen to implement several 28.75 mm diameter stacks appropriately wrapped in a Teflon tape to ensure sealing with the tube, a chosen length of 40 mm and a variable cross-sectional geometry. At the end of the optimization process, 19 stacks have been developed and created; their description is reported in Section 5. An arbitrary chosen length of 40 mm and a variable cross-sectional geometry was adopted in the beginning of the study. The length was first chosen for economical and easy reproductible reason. As it is shown in literature, samples with same kind of material properties at around 40 mm are quite optimal (Setiawan and Utamo, 2009). It is also easy to print with any standard 3D printer without any deformation of the stack. Under these conditions, if the stack is shorter or longer, it seems that the phenomenon is less efficient. This point will be verified experimentally in the subSection 4.3.

2.3. Measurement description

One of the aims of this study, as previously underlined, is to present repeatable, robust and comparable processes and results. One of the most challenging aspects of the measurement setup was to ensure the exact position of the thermocouples in the tube for each test. During multiple measurements conducted before finding the correct thermocouples position, it was noted that even a small axial or radial displacement-shift in thermocouples position implied a slightly different recorded temperature, thus compromising the repeatability of the study. In order to ensure the accuracy and comparability of each measurement, each thermocouple has been fixed to the tube walls with a synthetic rubber compound and placed at the center of each stack edge section

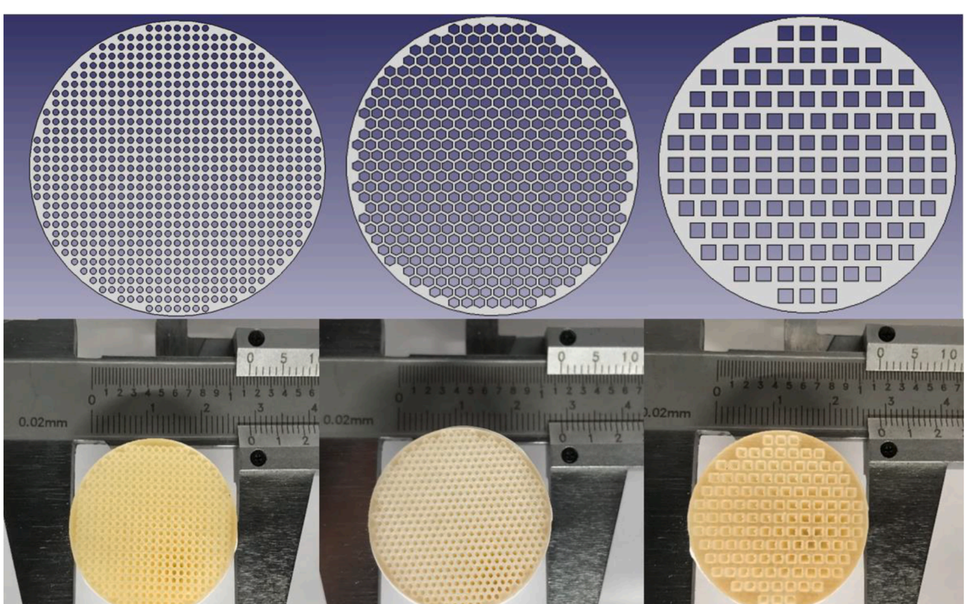

Fig. 3. Three different stack geometries (circular, honeycomb and square holes): sketch and printed samples.

(corresponding to 14.5 mm from the tube wall in each direction) at a distance of 1 mm from the stack side.

In order to ensure the accuracy of the study, each measurement has been conducted 5 times and under the same conditions, for a total of 95 acceptable measurements. The starting temperature at the beginning of each test has always been kept equal to the room temperature. i.e. 23 °C. Each measurement was carried out to last 1000 s, a time long enough to assure that the hot and cold temperature trends had always completed the transient period, settling on a constant asymptotical value. At the beginning of each test, the measurement started without any sound in order to ensure the temperature stability in the resonator tube; 30 s after the start of recording, the sound level amplitude was gradually set to the effective value needed for each test. A typical result obtained from the measurement tests is reported in Fig. 4, trend which is coherent to the ones found in literature (Mahamuni et al., 2015; Russel and Weibull, 2002), and in the studies of Swift and Crocker (Swift, 1999; Swift, 2002; Crocker, 1997).

It is possible to observe that at 1000 s the temperatures have settled to almost constant values, which have been considered the maximum temperature difference obtainable in each test. After each measurement, the stack was removed from the tube and replaced with another one, after a 15 min pause in order to let the air inside the resonator tube reach again room temperature, so that each measurement started at the same initial temperature conditions. Furthermore, in order to grant the reliability and the accuracy of the measurements, each test was carried out five times in five different days under the same conditions. At the end of the campaign, a mean temperature difference and its standard deviation were calculated for each stack.

In order to have a simple and understandable definition of the stacks, a nomenclature is introduced: concerning the geometry and the dimensional optimization process, since every stack is 40 mm long, the name of each stack is represented by a code A-B-C, where A is the stack pores geometry abbreviation, B is the material layer thickness in millimetres and C is the air gap spacing in millimetres corresponding to the pore dimension. When analysing the stack length optimization, the code modifies into A-B-C-D, where D is the stack length in millimetres. As an example, in Fig. 4 it is presented the temperature trend for the stack "sq-0.1–1–40″, meaning a stack with square pores geometry, a material layer 0.1 mm thick, an air square pore of 1 mm and a length of 40 mm.

3. Material characterisation

In order to obtain the maximum performance from the stack material in a thermoacoustic application, it should be characterised by a low thermal conductivity and a high specific heat capacity. In thermoacoustic refrigeration, two fundamental parameters are used to describe the bond between the acoustic and thermokinetic energy: the thermal penetration depth δ_t and the viscous penetration depth δ_v. The thermal penetration depth, defined as

$$\delta_t = \sqrt{\frac{k}{\pi f \rho c_p}} \tag{1}$$

represents the distance that the heat is able to diffuse through a gas in a time $t = \frac{1}{\pi} \cdot f$, being f the frequency of the sound wave, k the gas thermal conductivity, ρ the material density and c_p the material specific heat capacity. Another similar parameter is the viscous penetration depth δ_v, defined as

$$\delta_v = \sqrt{\frac{2\mu}{\omega \rho_m}} \tag{2}$$

Where μ is the fluid dynamic viscosity, ω is the angular frequency and ρ_m is the mean fluid density, and related to the thermal penetration depth by the Prandtl number by the following relation:

$$\delta_v = \delta_t \cdot \sqrt{Pr} \tag{3}$$

In literature, materials such as the one used in this study are usually characterized by means of their mechanical properties, but usually data about thermal properties is missing (see e.g. Dezaki et al., 2020). Since these thermal properties are not usually available for the catalog data of materials for 3D printers, it was necessary to obtain them

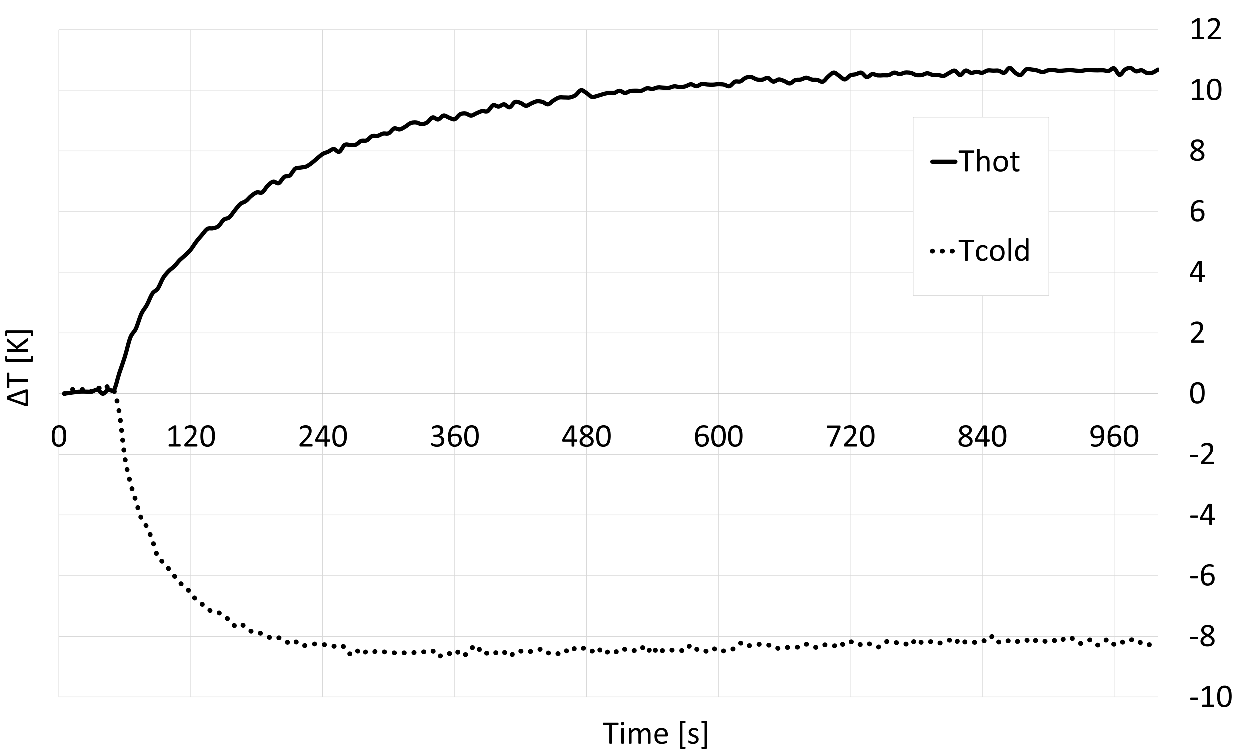

Fig. 4. Typical temperatures trend during a 1000 s measurement test (case sq-0.1–1–40).

experimentally. In this study the conductivity of the material was determined by means of a conductivity meter, whereas the specific heat capacity with an effusivity meter. To be more specific, a FP2C Neotim conductivity meter used in a transient hot wire method and a FP2C Neotim effusitvity meter used in a transient hot plane method were used to evaluate the properties of the "Visijet® M3 Crystal" printer material. Four different material specimens were printed, and every property was tested multiple times on each of them; then, an average value was calculated. The measurements gave a conductivity equal to 0.167 W/(m·K) and a specific heat capacity of 1928 J/(kg·K). Finally, the density of the material was determined with a LS220A Precisa high precision balance. The measured properties are fully satisfactory and certify the suitability of "Visijet® M3 Crystal" for thermoacoustic uses, in accordance with Swift (Swift, 1999; Swift and Garrett, 2003). A low thermal conductivity along the resonator results in no useful heat dissipation along the stack, and a material specific heat capacity higher than the one of the operating fluid facilitates the process of heat transfer from the source to the surface of the stack. With these data, it was possible to determine the thermal penetration depth as a function of the material thermal conductivity, density, specific heat capacity and of the tube resonance frequency. The obtained properties values are summarized in Table 1:

There are several studies in the literature (Zolpakar et al., 2017; Krstic et al., 2020; Kozuka et al., 2014; Bekkulov et al., 2020) on stacks produced with rapid prototyping polymers. Among these, Mylar (Zolpakar and Ghazali, 2019; Tijani et al., 2002c; Nurudin, 2008) appears to be the best, however presenting a lower specific heat capacity and slightly higher thermal conductivity than the Visijet® M3 Crystal considered in this study.

An estimate of the production costs of a stack was made. In addition to the cost of instrumentation, 3D printer, and electricity, and considering the price of the material used, a cost of about 1.70 €/stack should be expected for the Visijet® M3 Crystal material and about 0.30 €/stack for the wax backing.

4. Stack optimization process

This section deals with the optimization of the stack in order to achieve an optimal configuration. The optimization process is very tangled and faceted, since the parameters involved in thermoacoustics are many and complex (Raut et al., 2017; Tartibu, 2015). In order to ensure the cost-effectiveness and ease of replicability of the study, some parameters were not considered in the optimization, and other parameters were limited by technical requirements of the experimental setup. First, a higher amplitude provides higher pressure and consequently higher temperature values. Due to technical limitations related to the characteristics of the available loudspeaker, a constant amplitude value was maintained for all tests and for all stacks used. The position of the stack, unlike what reported in other studies (e.g. Sari et al., 2014), was not optimized because it was known a priori where the maximum pressure was located within the resonator, thus determining the ideal position. The local oscillation of air particles exposed to an acoustic wave causes a series of compressions and expansions that result in a release and absorption of heat from and to the surrounding environment. This phenomenon is of particular interest inside a stack because the geometry and size of the interstices greatly influences the propagation of the waves and, as a consequence, its temperature gradient on both sides. For this reason, in this study tubular structure of the stack pores was used in order to optimize their geometry and size. An optimization of the pore geometry (4.1) was implemented at first, and then an optimization of the pore size and pore spacing (4.2) followed. Finally, the stack length was optimized (4.3). A comparison with the results obtained by a numerical simulation with DeltaEC (Design Environment for Low-amplitude Thermo-acoustic Energy Conversion) version 6.4b2.7 software is presented in Section 4.4, in order to validate the experimental results. In Fig. 5 is reported the trend of the temperature difference achieved fo all the tested geometries.

Table 1
VisiJet® M3 Crystal thermophysical properties.

Property	Value
Density $[kg/m^3]$	1170
Thermal Conductivity $[W/(m{\cdot}K)]$	0.167
Effusivity $[(W{\cdot}S^{1/2})/(m^2{\cdot}K)]$	614.5
Specific Heat Capacity $[J/(kg{\cdot}K)]$	1927.98
Thermal Penetration Depth $[m]$	1.104E-05

4.1. Geometry optimization

Many different geometries have been analyzed in the literature, among which the parallel plate or pin array geometries are considered among the best ones (Rahpeima and Ebrahimi, 2019; Hariharan et al., 2012; El-Rahman et al., 2017; Nayak et al., 2017), and also numerical geometrical optimization can be found (Zink et al., 2009). However, due to the structural limitations of 3D printing, these geometries are complex to print with good accuracy, as the printed stack usually results structurally deformed and irregular, and for this reason these geometries were not considered in this study.

The first step of the stack optimization process consisted in finding the most efficient pore geometry. To do so, a comparison of three stacks of the same dimensions but with three different pore geometries was carried out. As presented in Fig. 6, the geometries considered are square, circle and honeycomb (hexagonal). In order to guarantee an exact symmetry of the stack design, the same pores dimension (B) and material gap between two adjacent pores (C) have been maintained along the section. The pore dimension corresponds namely to the square side, to the circle diameter and to the longest diagonal of the hexagon. For this optimization two different dimension stacks have been printed for each geometry: one stack presenting 1 mm pore dimension and 0.1 mm material gap and another one with a 1 mm pore dimension and a 0.25 mm material gap.

The most relevant result to be obtained was not just the temperature difference absolute value, but to understand the optimal pore geometry for a configuration of the same size which allowed the maximum temperature difference.

As represented in Fig. 7 and in Table 2, it can be noticed that in every considered configuration all presenting an air gap of 1 mm the highest temperature difference was obtained with the square geometry, followed by the honeycomb and then, with a consistent gap, by the circular geometry,. The square geometry allows for even pore spacing, not leaving large amounts of solid material as is the case with circular pores. Although honeycomb geometry also has the same quality, it is more imprecise than square geometry from an additive manufacturing point of view. Other geometries such parallel plates, considered the ones with the best overall performance by some authors as already said, have been found to be impossible to print with the 3D printing technology available by the authors. For this reason, it was decided to implement and deepen the square pore geometry.

Having chosen the square configuration as the most effective, the next step of the optimization dealt with the search for the best pore dimension and material thickness in order to obtain the best possible stack performance.

4.2. Dimension optimization

Once the square geometry was chosen, although other studies present optimal size values that are anyway not applicable to our setup geometry (Tijani et al., 2002c), an optimization of the square pores and material gap dimensions was implemented. The dimensional characteristics of the stacks considered in this section are summarized in Table 3. From a theoretical point of view, the best configuration with a

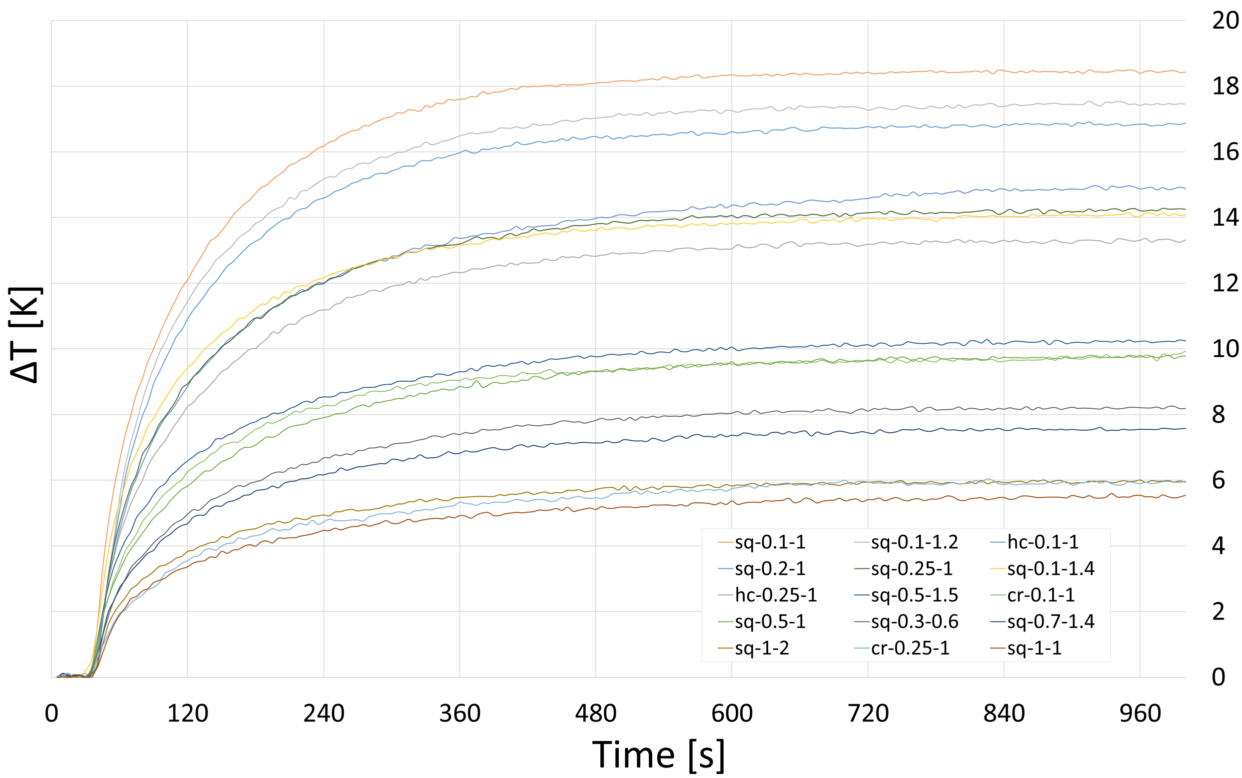

Fig. 5. Trend of the temperatures differences for all the test cases analyzed.

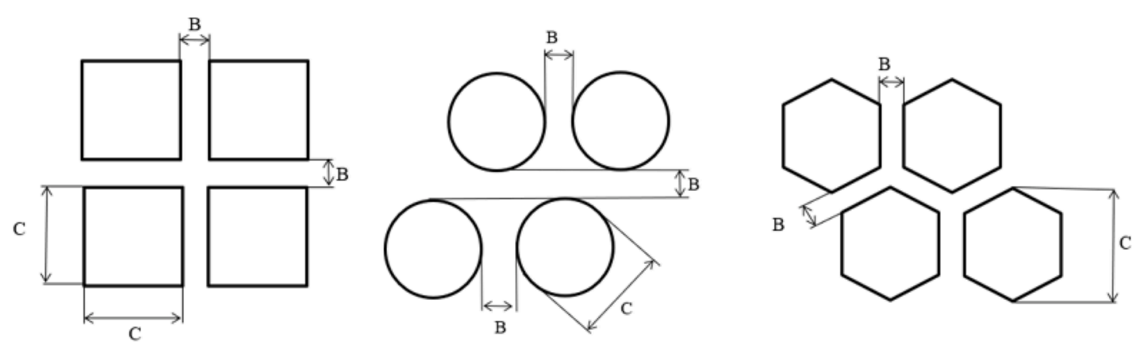

Fig. 6. Implemented stack pores geometries: (a) Square, (b) Circle and (c) Honeycomb.

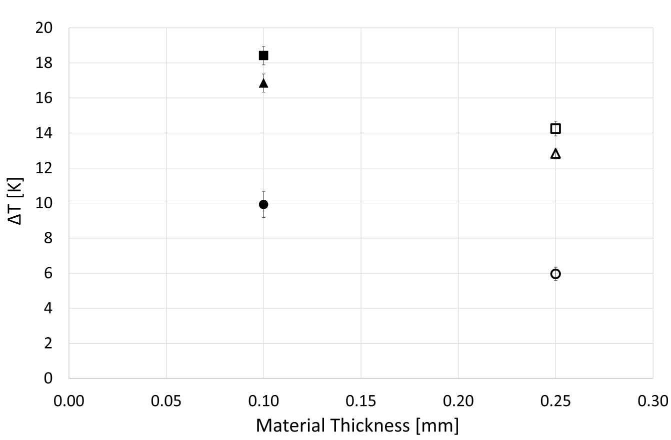

Fig. 7. Stack pores geometry optimization experimental results.

stack presenting a very thin material layer compared to the pores dimension was expected to be found, and in the following the most proper dimension and ratio among the materials and the air gaps is investigated and presented.

For a square geometry, the highest temperature difference, corresponding to 18.42 K, was measured for the configuration presenting a 0.1 mm material layer thickness, a 1 mm side square pore geometry and a 40 mm length. This configuration has a material layer size of 10 thermal penetration depths and an air-to-material ratio of 10.

A 3D printed stack having a material layer thickness lower than 0.1 mm will led to deformations during both the printing phase and the post-heating process, thus undermining the usability of the stack. Considering these structural and dimensional aspects, the optimum stack resulted to be the sq-0.1–1. In Fig. 8 the optimization process considering four different stack dimensions is presented: in particular, the mean temperature difference curves and envelope areas of the 5 tests conducted for each stack is shown.

As it can be noticed, all standard deviations obtained are below unity, confirming the robustness of the experimental procedure. In addition to measured temperature differences very similar for each

Table 2
Stack geometry optimization.

Name	Geometry	Material thickness [mm]	Mean ΔT [K]	1.96*Standard Deviation
cr-0.25–1	Circle	0.25	6.04	0.38
cr-0.1–1	Circle	0.1	9.91	0.75
hc-0.25–1	Honeycomb	0.25	12.83	0.31
hc-0.1–1	Honeycomb	0.1	16.87	0.52
sq-0.25–1	Square	0.25	14.25	0.42
sq-0.1–1	Square	0.1	18.42	0.52

Table 3
Stack square geometry dimension optimization.

Name	Geometry	Material thickness [mm]	Air Gap [mm]	Mean ΔT [K]	1.96*Standard Deviation
sq-0.5–1	Square	0.5	1	9.78	0.46
sq-0.7–1.4	Square	0.7	1.4	7.57	0.70
sq-1–1	Square	1	1	5.53	0.69
sq-0.3–0.6	Square	0.3	0.6	8.18	0.40
sq-1–2	Square	1	2	5.93	0.58
sq-0.5–1.5	Square	0.5	1.5	10.24	0.74
sq-0.25–1	Square	0.25	1	14.25	0.42
sq-0.2–1	Square	0.2	1	14.88	0.70
sq-0.1–1	Square	0.1	1	18.42	0.52
sq-0.1–1.2	Square	0.1	1.2	17.45	0.42
sq-0.1–1.4	Square	0.1	1.4	14.06	0.48

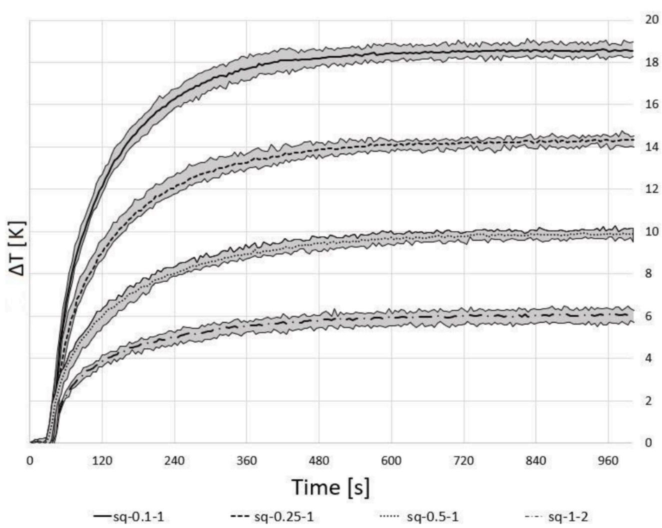

Fig. 8. Square geometry stack dimension optimization experimental results: measured mean temperatures and envelope curves.

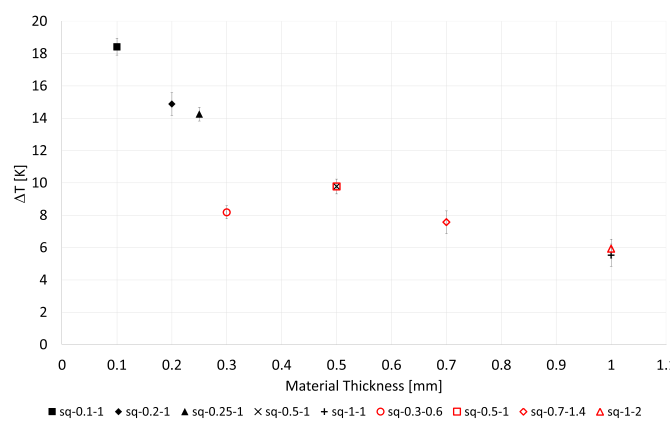

Fig. 9. Stack dimensions optimization: red markers represent the optimization at constant air/material ratio equal to 2, and black markers represent the material gap optimization at 1 mm constant air gap. (For interpretation of the references to colour in this figure legend, the reader is referred to the web version of this article.)

measurement, also the transient and the stationary parts of the temperature trends were really comparable.

In Fig. 9 two other different steps of the optimization can be observed: given the same air-to-material ratio equal to 2 (red markers), an optimal dimension was found in the sq-0.5–1 configuration, results that led to a study of different material gap thicknesses for a constant 1 mm square pore side (black markers).

Since the first three stacks already implemented, sq-0.1–1, sq-0.25–1 and sq-0.5–1, we studied the temperature difference trend by adding the sq-0.2–1 and sq-1–1 configurations in order to have different air-to-material ratios to compare. As previously said, the sq-0.1–1 configuration set a structural limit for the optimization process, and the sq-1–1 configuration had the lowest temperature difference found in the study, which did not encourage printing stacks with a higher material thickness. To complete the optimization, it was decided to print stacks with the optimal material thickness layer of 0.1 mm with a larger square pore side of 1.2 mm and 1.4 mm. The results obtained show lower temperature differences than the sq-0.1–1 configuration, confirming this combination of parameters as the optimal stack in terms of geometry and dimensions.

4.3. Length optimization

Having determined that the optimal stack is sq-0.1–1, stacks of different lengths were printed with this configuration. Stack length optimization, as presented by other authors (Alcock et al., 2018), results to be crucial in the optimization process of a stack. Since the first part of the optimization was only conducted for a 40 mm stack length, presenting a fixed air gap of 1 mm, four other stacks of varying lengths of 20 mm, 30 mm, 50 mm, and 60 mm were considered, as shown in Table 4.

The limit for optimization was set at 60 mm due to the technical limitation of the 3D printer used in this study, that led to an axial deformation for longer stacks during the printing phase. From an experimental point of view, given the different stack lengths, the position of the hot side and its thermocouples were kept at 1 cm from the edge of the resonator to achieve maximum pressure, and the cold side

Table 4
Optimized square 0,1–1 stack length optimization.

Name	Geometry	Length [mm]	Mean ΔT [K]	1.96*Standard Deviation
sq–0.1–1–20	Square	20	13.35	0.94
sq–0.1–1–30	Square	30	14.47	0.53
sq–0.1–1–40	Square	40	18.42	0.52
sq–0.1–1–50	Square	50	15.49	0.56
sq–0.1–1–60	Square	60	12.50	0.75

thermocouples were appropriately shifted according to the stack length while maintaining the same spatial position corresponding to the center of the stack section, always at the same distance from the stack edge. After a campaign of 5 measurements for each stack under the same conditions, it was noted that the 40 mm stack had the maximum temperature difference achieved for the resonator dimension considered in this study. As observed in Fig. 10, the optimization trend shows that both shorter and longer stacks have lower levels of ΔT, trend which could also be observed in other studies conducted (Setiawan and Utamo, 2009).

4.4. Comparison with DeltaEC model and final considerations

Finally, a numerical model was implemented by using the thermoacoustic software Design Environment for Low-amplitude Thermoacoustic Energy Conversion (DeltaEC) software (Ward et al., 2017).

A standing wave duct with the same geometry and characteristics as the existing experimental setup was simulated, and the schematic can be seen in Fig. 11; the components in the schematic are numbered as follows:

0. "BEGIN" segment with initial values;
1. "SURFACE" area with thermal-hysteresis dissipation;
2. "DUCT" segment describing the initial part of the circular duct;
3. "STKRECT" used to describe the stack with square pores (circular and hexagonal pores were otherwise both simulated with the appropriate "STKCIRC" component in DeltaEC);
4. "DUCT" segment describing the final part of the circular duct;
5. "HARDEND" final segment representing the end of the closed thermoacoustic system, where the complex volume flow rate is equal to zero.

The fundamental geometrical parameters for the numerical simulation were based on purely experimental and original data from the study, such as the number of pores in each stack, a function of the stack cross-sectional dimensions and the characteristic pore lengths and distances between them. The first numerically simulated case was the optimal stack sq-0.1–1–40. In order to verify the correctness and

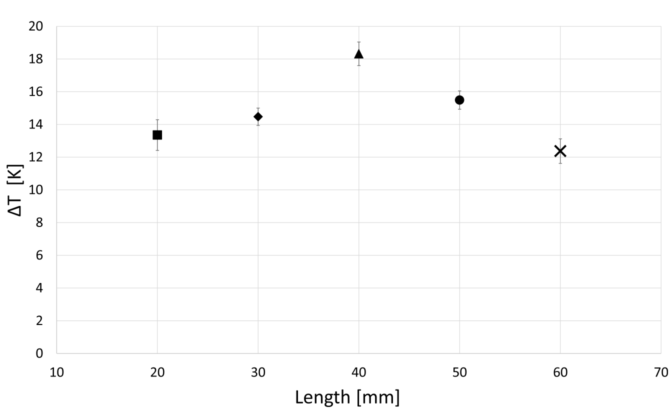

Fig. 10. Optimized stack sq-0,1–1 length optimization experimental results.

applicability of the model to all stack geometries, the same general data (i.e. physical quantities) were maintained in each simulation, while the geometrical characteristic parameters of each stack were varied (i.e. geometry, number of pores, pore size, distance between them). Fig. 12 shows a comparison of the temperature difference data obtained experimentally (X-axis) and numerically (Y-axis) for 40 mm long square stacks with different pore configurations and sizes.

The bisector, which indicates the ideal correspondence between the calculated and the measured data, shows the good agreement of the numerical model with the experiments, where and all results except one deviate from the ideal case by a maximum margin of $\pm$ 2 K. The only case outside this zone is the sq-0.1–1.4–40 case, for which the numerical simulation predicts a higher ΔT than that experimentally found. This may be due to the fact that this stack represents a structurally borderline case (air/material ratio equal to 14), in which the print exhibits slight deformations due to the thin and loosely packed structure of the inner lattice of the stack, which may have influenced a lower experimental result. Generally speaking, the results obtained numerically are usually higher than those found experimentally, even if by small values, most likely due to slight imperfections in the printing and experimental setup. In spite of this, the numerical model can be considered valid, as it provides a priori a correct trend with a minimal deviation of the ΔT obtainable, matching the precise trend of the results obtained experimentally.

5. Conclusions

A description of an inexpensive, simple, robust, and replicable standing wave thermoacoustic refrigerator was presented in this paper. In particular it was possible to perform an optimization of the same in order to find the highest possible temperature gradient to be included in a hypothetical refrigeration cycle, by focusing on the material, the production and the characteristics of the 3D printed manufactured stacks. Starting from an optimization between three different geometries, it was found that the pores with square geometry gave better results than similar stacks with circular and honeycomb geometries. Although geometries and configurations with better results can be found in literature, the square geometry was chosen because of the excellent results found and the simplicity of realization with the technique developed in this study, which makes it difficult to print other geometries, such as parallel plates. Then, after an analysis of 11 different square pore configurations and 5 different lengths, the optimal stack resulted to have square pores with 1 mm side and 0.1 mm spacing and a length of 40 mm, presenting a temperature difference of 18.32 K at the edges of the stack itself. A numerical model was also developed, using the DeltaEC thermoacoustic software. Being the goal of this study to develop a clear procedure in order to obtain in 3D printed stacks tin a fast and not expensive way, the focus was on the obtainable temperature difference only, and heat exchangers were not taken into account: this aspect will be the part of future studies, that will also focus on other specific numerical simulations, by means of FEM softwares, that would allow a more precise definition of some specific parameters to be used for simulations. In this case, theoretical based non-dimensional parameters will be used (e.g. hydraulic diameter), since this approach will lead to better comparisons without the need to keep the geometrical dimensions of the samples too simple due to the constraints of the additive manufacturing technologies. Nevertheless, the numerical model, developed and validated by the experimental data, represented in a very accurate way the behavior of the stacks produced by additive manufacturing, proving itself to be a fast and economical way to help the rapid prototyping and to achieve a proper design and tuning of the stacks before proceeding to the 3D printing process.

Declaration of Competing Interest

The authors declare that they have no known competing financial

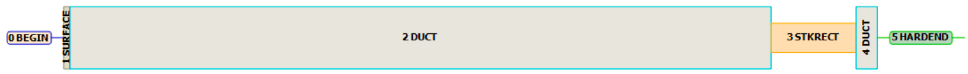

Fig. 11. DeltaEC calculation schematic.

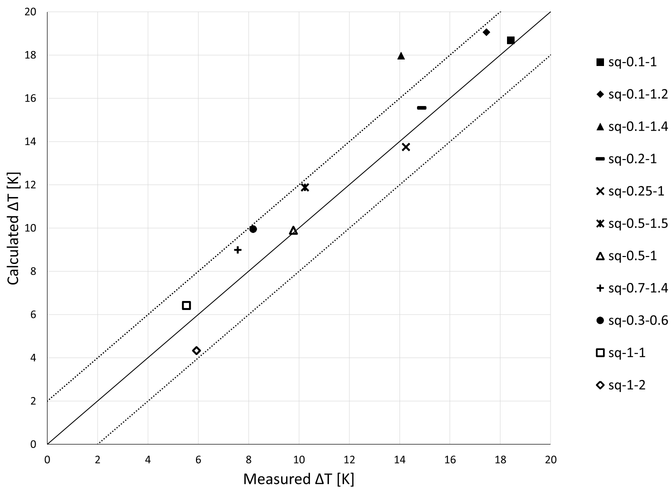

Fig. 12. Comparison between experimental results and DeltaEC simulation tests results in 40 mm square stacks with an error bandage of ± 2 K.

interests or personal relationships that could have appeared to influence the work reported in this paper.

Acknowledgements

This work was developed with the support of the Erasmus+ Programme for Study of the European Union. A learning agreement between the sending institution, the University of Genoa, in the person of Professor Davide Borelli, and the receiving institution, ENTPE, in the person of Professor Emmanuel Gourdon, allowed Emanuele Sarpero to spend a semester at ENTPE's LTDS laboratory and carry out the experimental campaign that led to the results reported in this article.

This work was carried out within the LABEX CeLyA (ANR-10-LABX-0060) of the University of Lyon, within the framework of the "Investissements d'Avenir" programme of the French government, managed by the Agence Nationale de la Recherche (ANR).

References

Alcock, A.C., Tartibu, L.K., Jen, T.C., 2017a. Design and construction of a thermoacoustically driven thermoacoustic refrigerator. In: 2017 International Conference on the Industrial and Commercial Use of Energy (ICUE), pp. 1–7. https://doi.org/10.23919/ICUE.2017.8103430.

Alcock, A.C., Tartibu, L.K., Jen, T.C., 2017b. Experimental investigation of ceramic substrates in standing wave thermoacoustic refrigerator. Procedia Manuf. 7, 79–85.

Alcock, A.C., Tartibu, L.K., Jen, T.C., 2018. Experimental investigation of an adjustable thermoacoustically-driven thermoacoustic refrigerator. Int. J. Refrig. 94, 71–86.

Allesina, G., 2014. An experimental analysis of a stand-alone standing-wave thermoacoustic refrigerator. Int. J. Energy and Environ. Eng. 5, 4, 2014.

Bekkulov, A., Luthen, A., Xu, B., 2020. Thermoacoustic cooler with various 3D-printed regenerators using water vapor as the working fluid. J. Energy Resour. Technol. Copyright. © 2019 by ASME MAY 2020, Vol. 142 /050904-1.

Berson, A., Poignand, G., Jondeau, E., Blanc-Benon, P., Comte-Bellot, G., 2012. Measurements of temperature and velocity fluctuations in oscillating flows using thermal anemometry application to thermoacoustic refrigerators. Societe Francaise d'Acoustique. Acoustics 2012. Apr 2012, Nantes, France. 2012. <hal-00811312>.

Bessis, R., Poignand, G., Bailliet, H., Lazure, H., Valiere, J.C., Boudard, E., 2015. Dual thermoacoustic core compact heat-pump for automotive application. DOI: 10.3990/2.309. In: Conference: Third international workshop on thermoacoustics.

Bhansali, P., Patunkar, P., Gorade, S., Adhav, S., Botre, S., 2015. An overview of stack design for a thermoacoustic refrigerator. IJRET: Int. J. Res. Eng. Technol. 04 (06).

Crocker, M.J., 1997. Handbook of Acoustics. Wiley, New York part 46 "Thermoacoustic Engines" by G.S Swift.

Debojit, R., Sandip, G., 2021. An experimental study on the effect of various stack materials on thermoacoustic refrigeration effect. J. Phys. Conference Series 2070 012220.

Dezaki, M.L., Ariffin, M.K.A.M., Appalanaidoo, D.A.I., Wahid, Z., Rage, A.M., 2020. 3D printed object's strength-toweight ratio analysis for M3 liquid material. Advances in Materials and Processing Technologies. https://doi.org/10.1080/2374068X.2020.1860596.

El-Rahman, A.I.A., Abdelfattah, W.A., Fouad, M.A., 2017. A 3D investigation of thermoacoustic fields in a square stack. Int. J. Heat and Mass Transf. 108 (2017), 292–300.

Garrett, S.L., Adeff, J.A., Hofler, T.J., 1993. Thermoacoustic refrigerator for space applications. J. Thermophys. Heat Transf. 7 (4), 595–599 (ISSN 0887-8722).

Hariharan, N.M., Sivashanmugam, P., Kasthurirengan, S., 2012. Influence of stack geometry and resonator length on the performance of thermoacoustic engine. Appl. Acoustics 73 (2012), 1052–1058.

Jebali, F., Lubiez, J.V., Francois, M.X., 2004. Response of a thermoacoustic refrigerator to the variation of the driving frequency and loading. Int. J. Refrig. 27 (2), 165–175. VolumeMarch.

Jin, T., Chen, G., Wang, B., Zhang, S., 2003. Application of thermoacoustic effect to refrigeration. Rev. Sci. Instrum. 74 (1), 677–679.

Kozuka, T., Yasui, K., Yasuoka, M., Kato, K., Sakamoto, S., 2014. Study of a stack made bu a 3D printer in the thermoacoustic system. Proceed. Symposium on Ultrasonic Electron. 35, pp. 123-1243-5 December 2014.

Krstic, A., Gagne, Z., Boylan, P., Franks, K., Boland, C., Jahncke, I., Gerchikov, T., Hillier, J., 2020. Designing and manufacturing a thermoacoustic refrigerator. J. Undergrad. Eng. Phys. Phys. Exp. Queens 1. Section 3April.

Mahamuni, P., Bhansali, P., Shah, N., Parikh, P., 2015. A Study of Thermoacoustic Refrigeration System. Int. J. Innovative Res. Adv. Eng. (IJIRAE) 2 (2). ISSN: 2349-2163 (IJIRAE)February.

Nayak, B.R., Bheemsha, B., Pundarika, G., 2015. Performance evaluation of thermoacoustic refrigerator using air as working medium. SSRG Int. J. Therm. Eng. (SSRG-IJTE) 1 (2). May to Aug.

Nayak, B.R., Pundarika, G., Bheemsha, A., 2017. Influence of stack geometry on the performance of thermoacoustic Refrigerator. Sadhana 42 (2), 223–230. February.

Nurudin, B.H.M.A, 2008. Thermal Performance of a Thermoacoustic Stack. Faculty of Mechanical Engineering Universiti Teknologi Malaysia.

Poese, M.E., Smith, R.W.M., Garrett, S.L., Van Gerwen, R., Gosselin, P., 2004. Thermoacoustic Refrigeration For Ice Cream Sales. The Pennsylvania State University Applied Research Laboratory, Penn State University.

Rahpeima, R., Ebrahimi, R., 2019. Numerical investigation of the effect of stack geometrical parameters and thermo-physical properties on performance of a standing wave thermoacoustic refrigerator. Appl. Therm. Eng. 149 (2019).

Ramadan, I.A., Bailliet, H., Poignand, G., Gardner, D., 2021. Design, manufacturing and testing of a compact thermoacoustic refrigerator. Appl. Therm. Eng. 189 (2021), 116705.

Raut, A.S., Wankhede, U.S., Walke, P.V., 2017. Design and optimization of stack for EcoFriendly thermoacoustic refrigeration system. IJSTE - Int. J. Sci. Technol. Eng. 4 (6). December.

Rossing, T.D., 2007. Springer Handbook of Acoustic. Stanford University, Center for Computer Research in Music and Acoustics, Stanford, CAUSA, 94305section 7 "Thermoacoustics".

Russel, D.A., Weibull, P., 2002. Tabletop thermoacoustic refrigerator for demonstrations. Am. J. Phys. 70 (12), 1231–1233.

Sari, P.D., Putea, I.B.A., Hendradjit, W., 2014. Effects of stack position on the optimum performance of a thermo-acoustics refrigeration system using ABS (Acrylonitrile Butadiene Styrene) stack material. In: 7th International Conference on Physics and Its Applications 2014.

Setiawan, I., Utamo, A.B.S., 2009. The influence of the length and position of the stack on the performance of a thermo acoustic refrigerator. Physics Dep. Gadjah Mada Uni. Sekip Ultra BLS 21 Yogyakarta 55281. Indonesia.

Shah, V.S., Parekh, A.K., Pandya, K.T., Bhavsar, M.R., Kapadia, R.G., 2021. Analysis of thermo-acoustic refrigeration system. Int. Res. J. Eng. Technol. (IRJET) 08 (08). Aug 2021.

Swift, G.W., 2002. Thermoacoustic: A Unifying Perspective for Some Engines and Refrigerators. Springer, Los Alamos National Laboratory.

Swift, G.W., 1999. Thermoacoustic: engines and refrigerators, a short course. In: Joint 137th Meeting of Acoustical Societies of America and Europe.

Swift, G.W., Garrett, S.L., 2003. Thermoacoustics: a unifying perspective for some engines and refrigerators. J. Acoust. Soc. Am. 113, 2379–2381.

Tartibu, L.K., 2015. Maximum cooling and maximum efficiency of thermoacoustic refrigerators. Heat Mass Transfer DOI 10.1007/s00231-015-1599-y. Springer-Verlag Berlin Heidelberg, 2015.

Tijani, M.E.H., Zeegers, J.C.H., de Waele, A.T.A.M., 2002a. Design of thermoacoustic refrigerators. Cryogenics 42, 49–57.

Tijani, M.E.H., Zeegers, J.C.H., De Waele, A.T.A.M., 2002b. Construction and performance of a thermoacoustic refrigerator. Cryogenics 42 (1), 59–66.

Tijani, M.E.H., Zeegers, J.C.H., de Waele, A.T.A.M., 2002c. The optimal stack spacing for thermoacoustic refrigeration. J. Acoust. Soc. Am. 112 (1) https://doi.org/10.1121/1.1487842.

Ward, B., Clark, J., Swift, G., 2017. Design Environment for Low-amplitude Thermoacoustic Energy Conversion DeltaEC Version 6.4b2.7 Users Guide. Los Alamos National Laboratory. LA-CC-01-13, LA-CC-16-053. Available online. https://www.lanl.gov/org/ddste/aldps/materials-physics-applications/condensed-matter-magnet-science/thermoacoustics/_assets/docs/UsersGuide.pdf.
Wetzel, M., Herman, C., January 1997. Design optimization of thermoacoustic refrigerators. Int. J. Refrig. 20 (1), 3–21.
Yahya, S.G., Mao, X., Jaworski, A.J., 2017. Experimental investigation of thermal performance of random stack materials for use in standing wave thermoacoustic refrigerators. Int. J. Refrig. 75, 52–63.
Zink, F., Waterer, H., Archer, R., Schaefer, L., 2009. Geometric optimization of a thermoacoustic regenerator. Int. J. Therm. Sci. 48, 2309–2322.
Zolpakar, N.A., Mohd-Ghazali, N., El-Fawal, M.H., 2016. Performance analysis of the standing wave thermoacoustic refrigerator: a review. Renew.Sustai. Energy Rev. 54 (2016), 626–634.
Zolpakar, N.A., Ghazali, N.M., Ahmad, R., Maré, T., 2017. Performance of a 3D-printed stack in a standing wave thermoacoustic refrigerator. In: The 8th International Conference on Applied Energy – ICAE2016.
Zolpakar, N.A., Ghazali, N.M., 2019. Comparison of a thermoacoustic refrigerator stack performance: Mylar spiral, celcor substrates and 3D printed stacks. In: International Journal of Air-Conditioning and Refrigeration, 27. World Scientific, 1950021.